



**HAL**  
open science

## How evolving multiaxial stress states affect the kinetics of rafting during creep of single crystal Ni-base superalloys

L. Cao, P. Wollgramm, D. Burger, A. Kostka, Georges Cailletaud, G. Eggeler

► **To cite this version:**

L. Cao, P. Wollgramm, D. Burger, A. Kostka, Georges Cailletaud, et al.. How evolving multiaxial stress states affect the kinetics of rafting during creep of single crystal Ni-base superalloys. *Acta Materialia*, 2018, 158, pp.381-392. 10.1016/j.actamat.2018.07.061 . hal-01869054

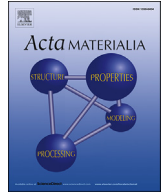
**HAL Id: hal-01869054**

**<https://minesparis-psl.hal.science/hal-01869054>**

Submitted on 6 Sep 2018

**HAL** is a multi-disciplinary open access archive for the deposit and dissemination of scientific research documents, whether they are published or not. The documents may come from teaching and research institutions in France or abroad, or from public or private research centers.

L'archive ouverte pluridisciplinaire **HAL**, est destinée au dépôt et à la diffusion de documents scientifiques de niveau recherche, publiés ou non, émanant des établissements d'enseignement et de recherche français ou étrangers, des laboratoires publics ou privés.



## Full length article

## How evolving multiaxial stress states affect the kinetics of rafting during creep of single crystal Ni-base superalloys

L. Cao <sup>a,\*</sup>, P. Wollgramm <sup>a</sup>, D. Bürger <sup>a</sup>, A. Kostka <sup>b</sup>, G. Cailletaud <sup>c</sup>, G. Eggeler <sup>a</sup><sup>a</sup> Institut für Werkstoffe, Ruhr-Universität Bochum, Universitätsstr. 150, 44801, Bochum, Germany<sup>b</sup> Zentrum für Grenzflächendominierte Höchstleistungswerkstoffe, Ruhr-Universität Bochum, Universitätsstr. 150, 44801, Bochum, Germany<sup>c</sup> Mines Paristech, PSL Research University, Centre des Matériaux, CNRS UMR 7633, 63-65 rue Henri Auguste Desbrières, 91003, Evry Cedex, France

## ARTICLE INFO

## Article history:

Received 16 April 2018

Received in revised form

25 June 2018

Accepted 26 July 2018

Available online 1 August 2018

## Keywords:

Single crystal Ni-base superalloys

Circular notched creep specimen

Stress redistribution

Kinetics of rafting

Evolution of dislocation substructure

## ABSTRACT

Miniature tensile creep specimens are used to investigate the effect of mild circular notches on microstructural evolution during [001] tensile creep of a Ni-base single crystal superalloy. Creep deformed material states from a uniaxial (950 °C, uniaxial stress: 300 MPa) and a circular notched creep specimen (950 °C, net section stress in notch root: 300 MPa) are compared. For both types of tests, creep experiments were interrupted after 81, 169 and 306 h. Quantitative scanning electron microscopy (SEM) is used to assess the evolution of the  $\gamma/\gamma'$ -microstructure from rafting to topological inversion. Scanning transmission electron microscopy (STEM) was applied to study the evolution of dislocation densities during creep. As a striking new result it is shown that in circular notched specimen, the microstructural evolution is well coupled to the kinetics of the stress redistribution during creep. Rafting, the directional coarsening of the  $\gamma'$ -phase, and the increase of  $\gamma$ -channel dislocation density, start in the notch root before the center of the specimen is affected. When stresses in the circular notched specimens are fully redistributed, the microstructural differences between the notch root and the center of the circular notched specimen disappear. The comparison of the mechanical data and the microstructural findings in uniaxial and circular notched specimens contribute to a better understanding of the role of mild notches, of stress multiaxiality and of strain accumulation in the microstructure evolution of single crystal Ni-base superalloys during creep. The results obtained in the present work are discussed in the light of previous work published in the literature.

© 2018 Acta Materialia Inc. Published by Elsevier Ltd. This is an open access article under the CC BY-NC-ND license (<http://creativecommons.org/licenses/by-nc-nd/4.0/>).

## 1. Introduction

Ni-base superalloy single crystals (SXs) are used to make blades for aero engines and gas turbines for power plants [1–4]. After processing and heat treatment, two macroscopic regions can be identified in the microstructure of Ni-base SX, which have their origin in segregation processes during solidification. Even after homogenization heat treatments one can distinguish between prior dendritic (D) and interdendritic regions (ID). Single crystal superalloys are produced using a Bridgman type or process, where the material solidifies in the <001> direction (growth direction of primary dendrites). A homogenization and precipitation heat treatment establishes a fine two phase microstructure in both regions. This microstructure consists of cuboidal  $\gamma'$ -particles (typical

volume fraction: 75%, typical average  $\gamma'$ -cube edge length: 0.5  $\mu\text{m}$ , crystal structure:  $L1_2$  phase) which are separated by thin  $\gamma$ -channels (typical volume fraction: 25%, typical average  $\gamma$ -channel width: 100 nm, crystal structure: fcc). The atoms of both phases occupy a common fcc lattice, where the lattice constant of the  $\gamma$ -channel phase  $a_\gamma$  is often larger than that of the ordered  $\gamma'$ -phase  $a_{\gamma'}$ . This gives rise to a negative lattice misfit  $\delta$  between the two phases:

$$\delta = (a_{\gamma'} - a_\gamma) / (1/2 \cdot (a_{\gamma'} + a_\gamma)) \quad (1)$$

Tensile loading of negative misfit alloys in <001> direction results in a directional coarsening of the  $\gamma'$ -phase, which is characterized by the formation of rafts perpendicular to the loading direction [3]. Rafting of the  $\gamma'$ -phase in Ni-based SXs is probably the best known microstructural instability in high temperature materials technology. The micromechanics, thermodynamics and kinetics of rafting have been theoretically e.g. Refs. [5–18] and

\* Corresponding author.

E-mail address: [Lijie.Cao@rub.de](mailto:Lijie.Cao@rub.de) (L. Cao).

experimentally e.g. Refs. [5,6,15–40] investigated. It has been shown that the evolution of a raft microstructure during creep depends on the lattice misfit e.g. Refs. [39,40] (which can cause misfit stresses as high as 500 MPa [19]), the crystallographic loading direction during uniaxial testing e.g. Refs. [27,28] and the nature of the multiaxial stress state during multiaxial loading [13,25–32]. Rafting also depends on local microstructural conditions like the features of the cast microstructure (D or ID region) e.g. Refs. [37,38] or the presence of elevated dislocation densities next to a hardness indent [20].

SX turbine blades have to withstand mechanical loads at elevated temperatures, where creep [41,42] limits their service life. Stress states can be multiaxial and therefore there is an interest in creep experiments which are performed under multiaxial states of stress [43,44]. One way of achieving a multiaxial stress state is to use circular notched tensile bars with mild notches [45–50]. It is well known that stresses redistribute in circular notched specimens during creep. Directly after loading, the initial condition reflects the elastic condition which is characterized by high stresses in the notch root and lower stresses in the center of the notched bar. With plastic deformation, stresses in the notched bar redistribute as has been investigated and discussed for plastic flow and creep conditions in Refs. [44–50]. Finite element creep stress analysis (FEM) provides insight into how stresses re-distribute during creep [45–48]. Recently a circular notched miniature tensile creep (CNMTC) specimen was designed [50], where this stress redistribution occurs within a few hundred hours at a temperature of 950 °C. The scientific objective of the present work is to find out, how this stress redistribution affects the evolution of the  $\gamma/\gamma'$ -microstructure and how rafting in a [001] CNMTC specimen (multiaxial stress state) compares to rafting in a [001] FUMTC (flat uniaxial miniature tensile creep) specimen (uniaxial stress state). Moreover, an effort is made to study the influence of stress states and strain accumulation on the dislocation substructure.

## 2. Material and experiments

### 2.1. Material and miniature creep testing

In the present study the single crystal superalloy ERBO1 (CMSX-4 type) is investigated. Its average chemical composition is given in Table 1. All details describing the heat treatment and the microstructure of ERBO1 are given elsewhere [51,52].

In the present work, miniature creep tests are performed on tensile specimens oriented in [001] direction. Tensile specimens with and without circular notches were investigated. The miniature creep test technique and all aspects concerning the creep data acquisition from uniaxial and circular notched tensile specimens have been described elsewhere [50,53]. In the present work six interrupted creep tests were performed at 950 °C and a net section stress of 300 MPa. In case of the flat uniaxial miniature tensile creep specimens (FUMTC specimens, see Fig. 3 of [53]), this stress corresponds to the uniaxial stress which is constant over the whole cross section of the specimen. The circular notched miniature tensile specimen is shown in Fig. 1a. It is subjected to stress redistribution during creep. Finite element creep stress analysis was performed in Ref. [50], to calculate this stress redistribution in the CNMTC specimen under the creep conditions imposed in the

present work. All details of the FEM procedure (software, elements, meshing, input parameters, creep law) are described in Ref. [50], where isotropic material behavior was assumed and creep was represented by a simple power law. It is sufficient for the scientific objectives of the present work. Results on stress redistribution during creep obtained using the procedure documented in Ref. [50] are presented in Fig. 1b and c. Fig. 1b shows how the maximum principal stress  $\sigma_1$  (which corresponds to the axial stress in loading direction) varies over the specimen cross section. It is plotted as a function of  $x/d$  where  $x$  is the position in the cross section and  $d$  is the notch root diameter.  $x/d$  values of 0 and 0.5 represent the notch root and the center of the CNMTC specimen, respectively. For reasons of symmetry there is no need to show the other half of the curve. Fig. 1b shows that the stress  $\sigma_1(x/d)$ -curves change strongly during creep. Directly after loading (elastic FEM solution) the notch root stress has a value of 419 MPa (which is in good agreement with the analytical solutions for the notch root [54–56]), and it decreases to 223 MPa in the center of the specimen.

After 306 h of creep the notch root value has decreased to 258 MPa while the center value has increased to 352 MPa. Fig. 1c shows how the hydrostatic stress  $\sigma_H$  and the von Mises effective stress  $\sigma_V$  (e.g. Ref. [56]) vary in the notch root cross section. Fig. 1c also shows how the  $\sigma_H(x/d)$  - and  $\sigma_V(x/d)$  -curves change under elastic loading and after 306 h of creep. Fig. 1d shows the distribution of the stress triaxiality  $\eta = \sigma_H/\sigma_V$  over half of the cross section. Under elastic loading the stress triaxiality increases from 0.43 in the notch root to 0.62 in the center, while it increases from 0.37 in the notch root to 0.76 in the center after 306 h of creep. All mechanical details of circular notched creep testing have been explained in Ref. [50].

Three FUMTC and three CNMTC specimens were tested under creep conditions for 81, 169 and 306 h, details are given in Table 2. The corresponding creep curves are shown in Fig. 10 of Ref. [50].

### 2.2. Metallographic cross sections and scanning electron microscopy

After creep testing, longitudinal cross sections of the specimens were prepared for investigation in a scanning electron microscope (SEM) of type Leo Gemini 1530 from Carl Zeiss AG. All details concerning the SEM work have been published elsewhere [27,28,38]. In case of the CNMTC specimens, the center lines of the specimens were fully contained in the SEM cross sections. Fig. 2a shows a schematic drawing of the longitudinal cross section of a CNMTC specimen, illustrating the four positions where SEM investigations were performed. Three locations were defined in the cross section of the notch root (1 - center, 2 - middle, 3 - surface). Location 4 represents a position along the central longitudinal loading axis of the specimen. A SEM micrograph of the notch region of the CNMTC specimen crept for 169 h is shown in Fig. 2b.

The low magnification SEM micrograph was taken using back scatter electron SEM contrast revealing a complexity associated with the large-scale heterogeneity which characterizes cast SX. Even after extended homogenization heat treatments one can distinguish between prior dendritic (D) and interdendritic (ID) regions in SX cast alloys. In Fig. 2b, D regions appear brighter. The solidification direction of SX materials corresponded to the [001] growth direction of primary dendrites (one primary dendrite is highlighted by a long vertical black arrow). The average dendrite spacing in our material was several hundred  $\mu\text{m}$  [51]. Therefore, only a few primary dendrites were present in the  $\langle 100 \rangle$  cross section of our CNMTC specimens. A small black horizontal arrow pointing to the right highlights the position of secondary dendrite arm. Dendritic and interdendritic regions can differ in chemical composition and in  $\gamma'$ -volume fractions [51,52]. Instead of simply

**Table 1**  
Average chemical composition of ERBO1 in wt.%.

Al	Co	Cr	Hf	Mo	Re	Ta	Ti	W	Ni
5.8	9.3	6.2	0.1	0.6	2.9	6.9	1.0	6.3	Bal.

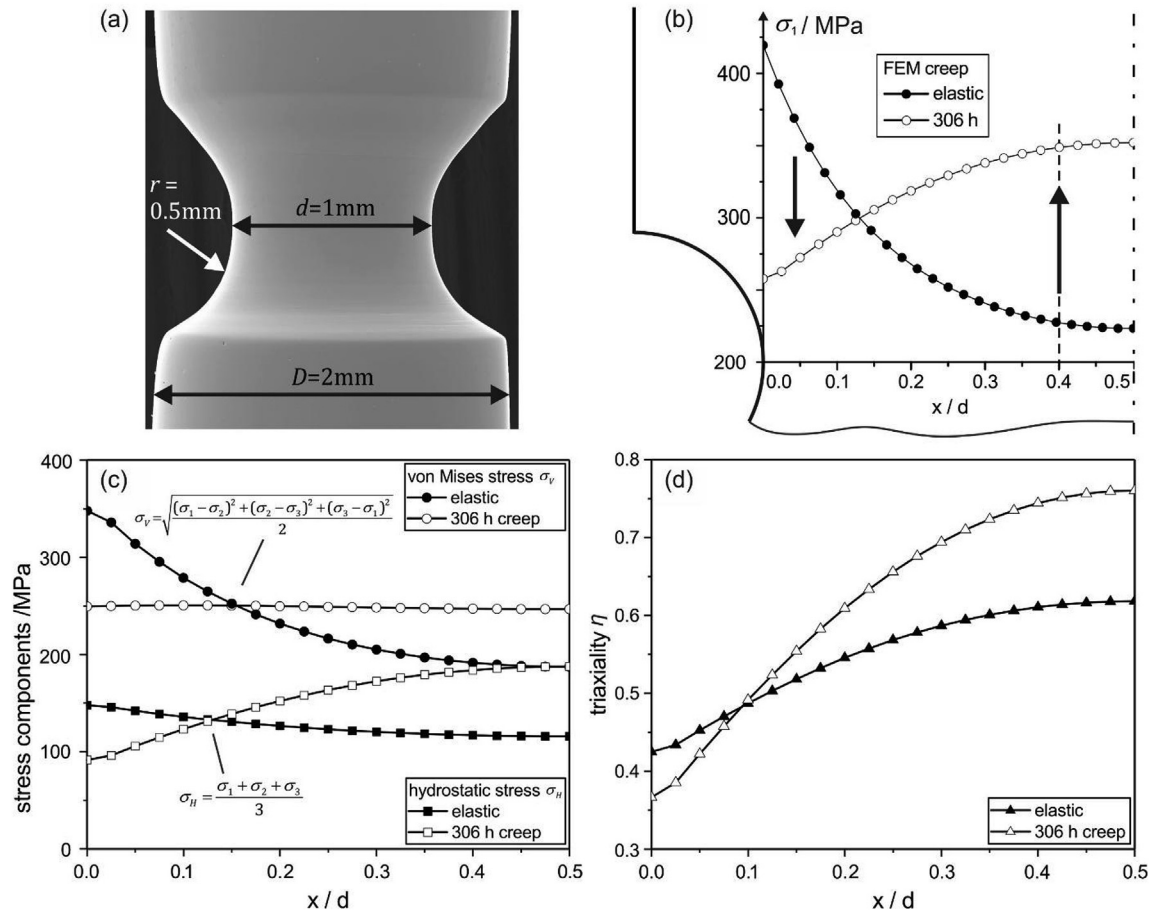


**Fig. 1.** Short overview summary of results reported in Ref. [50]. (a) Geometry of CNMTC specimen. (b) Dependence of maximum principal stress  $\sigma_1$  (corresponding to axial stress in loading direction) on  $x/d$ . Full circles: elastic FEM solution. Empty circles: 306 h of creep. (c) Dependence of von Mises effective stress (circles) and hydrostatic stress (squares) on  $x/d$ . Full symbol: elastic solution. Empty symbols: 306 h of creep. (d) Stress triaxiality  $\eta$  as a function of  $x/d$ . Full symbols: elastic solution. Empty symbols: 306 h of creep.

**Table 2**

Interrupted [001] tensile creep tests performed in the present work.

Specimen	Test type	Temperature [°C]	Net section stress [MPa]	Duration [h]	strain [%]
1	FUMTC	950	300	81	0.9
2	"	"	"	169	1.6
3	"	"	"	306	23.3
4	CNMTC	"	"	81	0.03 <sup>a</sup>
5	"	"	"	169	0.05 <sup>a</sup>
6	"	"	"	306	0.04 <sup>a</sup>

<sup>a</sup> Nominal macroscopic strains ( $\Delta L/L_0$ , strain measurement operating at limit of resolution; for details see Ref. [50]).

measuring  $\gamma'$ -sizes and shapes exactly at the locations defined in Fig. 2a, our measurements were performed considering the differences between dendritic and interdendritic regions. In Fig. 2b, the central position 1 was located close to the center of a dendrite. However, in other cases the target locations were not in dendritic regions. In these cases, measurements were performed in the dendritic region which was closest to the target location.

### 2.3. Quantitative metallography

In the present work, the following microstructural parameters were determined:  $\gamma'$ -volume fractions  $f_{\gamma'}$ ,  $\gamma$ -channel widths  $w$ ,  $\gamma'$ -particle sizes  $d$ , and a parameter  $R$  which quantifies the degree of topological inversion, as introduced by Epishin et al. [23] (Epishin-method). Fig. 3 shows SEM images taken from a circular notched

specimen after 169 h of creep exposure. The SEM image in Fig. 3a was taken from a dendritic region close to position 1 of Fig. 2a, where rafting was not yet apparent. In the present study, between 60 and 100  $\gamma$ -channels/ $\gamma'$ -particles were evaluated for each material state. A line intersection method is used to manually determine the  $\gamma'$ -volume fraction  $f_{\gamma'-LINE}$  based on the evaluation of the individual lengths of all line segments

$$f_{\gamma'-LINE} = \frac{\sum_{m=1}^p \Delta\gamma'_m}{\left( \sum_{m=1}^p \Delta\gamma'_m + \sum_{k=1}^r \Delta\gamma_k \right)} \quad (2)$$

where  $\Delta\gamma_k$  and  $\Delta\gamma'_m$  are the segment lengths associated with the width of the  $k$ th  $\gamma$ -channel and the size of the  $m$ th  $\gamma'$ -particle, respectively. Care was taken to ensure that the reference lines were positioned parallel to the direction of the applied load, and to avoid

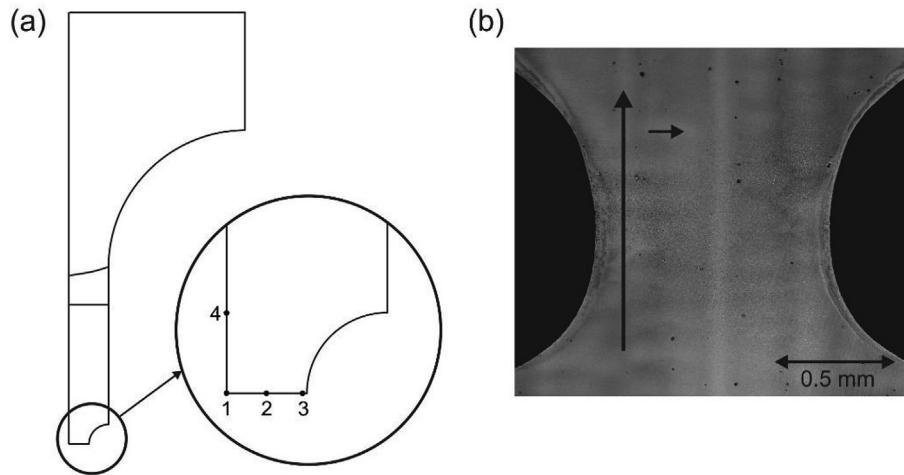


**Fig. 2.** Metallography of crept CNMTC specimens. (a) Four locations where SEM micrographs were taken. (b) SEM backscatter electron micrograph showing the longitudinal cross section in the center of the notch. For details see text.

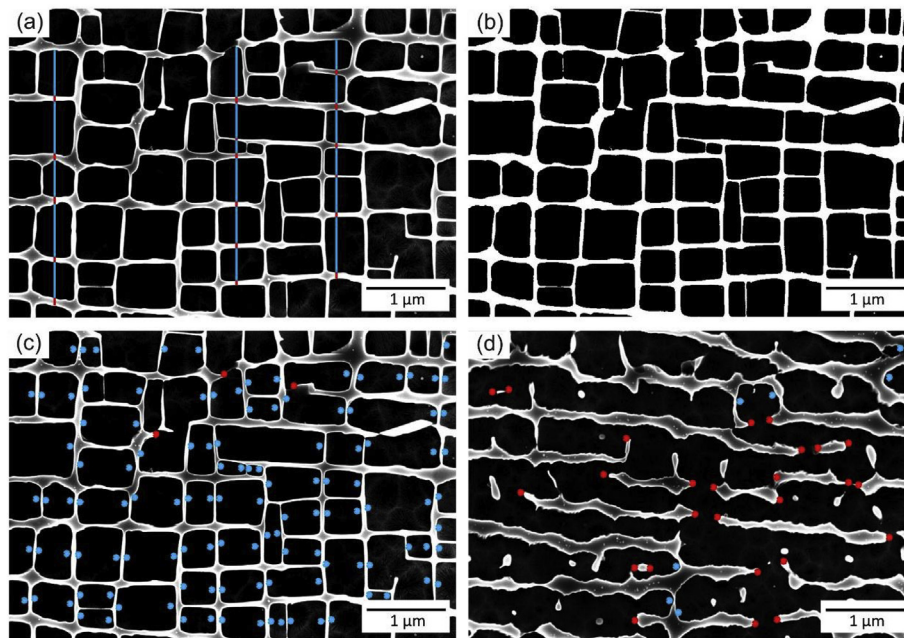


**Fig. 3.** Evaluation of SEM micrographs (CNMTC specimen, 950 °C, 300 MPa, 169 h). (a) SEM micrograph taken at position 1 highlighted in Fig. 2a with reference lines (parallel to the loading direction) for line intersection method. Blue/red line sections represent  $\gamma'/\gamma$ -regions respectively. (b) Binary image obtained from the SEM image shown in Fig. 3a. (c) SEM micrograph shown in Fig. 3a. The blue/red points represent terminations of the  $\gamma'/\gamma$ -phases as introduced by Epishin et al. [23] to quantify the topological inversion as outlined in Equation (6). (d) SEM micrograph taken at position 2 highlighted in Fig. 2a, where rafting is completed. The blue and red points are as described in Fig. 3c. For details see text.

a reference line being fully contained in a continuous vertical  $\gamma$ -channel.

The SEM micrograph from Fig. 3a was transformed into a binary image, Fig. 3b. This binary image was then evaluated using the software package *ImageJ*, which allowed to determine a projected area fraction of the  $\gamma'$ -phase  $f_{\gamma'-AREA}$ :

$$f_{\gamma'-AREA} = \sum_{i=1}^n a_i/A \quad (3)$$

where a total number of  $n$   $\gamma'$ -phase regions were distinguished on the SEM image.  $a_i$  represents the projected area of the  $i$ th  $\gamma'$ -particle and  $A$  represents the total area of the evaluated image.

Knowing the lengths of all line segments in both phases, it is

easy to evaluate an average  $\gamma$ -channel width  $\bar{w}$ .

$$\bar{w} = \sum_{k=1}^r \Delta\gamma_k/r \quad (4)$$

In order to quantify the microstructural scatter, the mean deviation  $\Delta\bar{w}$  from this mean value was calculated as

$$\Delta\bar{w} = \sum_{k=1}^r (|\bar{w} - \Delta\gamma_k|)/r \quad (5)$$

The same procedure yields an average value for the  $\gamma'$ -phase size  $\bar{d}$  (in loading direction) and the corresponding mean deviation from this mean value  $\Delta\bar{d}$ .

To quantify the degree to which the microstructure evolves from isolated  $\gamma'$ -cubes separated by thin  $\gamma$ -channels (e.g. Fig. 3a) to  $\gamma$ -islands in a  $\gamma'$ -matrix (early stage: Fig. 3d), the Epishin-method [19] was used. To apply this method, the numbers  $p'$  of terminations of the  $\gamma'$ -phase (blue points in Fig. 3c and d) and  $p$  of the  $\gamma$ -phase (red points in Fig. 3c and d) are counted. In the SEM micrograph of Fig. 3c, there are only a few red termination points of the  $\gamma$ -phase regions, at this stage the  $\gamma$ -phase is still continuous. In Fig. 3d, the number of the  $\gamma$ -terminations has significantly increased and the  $\gamma$ -phase has started to form isolated regions. The Epishin-parameter  $R$  is defined as

$$R = p/p' \quad (6)$$

It is clear that for the microstructure shown in Fig. 3c,  $R$  is close to 0. In contrast, for the microstructure shown in Fig. 3d it is significantly larger than 1. In the present work, we perform this evaluation for cross section regions of about  $300 \mu\text{m}^2$ .

#### 2.4. Scanning transmission electron microscopy (STEM)

In order to investigate dislocation structures, four electron transparent TEM foils were prepared from positions 1 (center of the specimen) and 3 (notch root) after 169 and 306 h creep testing ([001] CNMTC specimens 5 and 6 from Table 2). After testing, the specimens were first cut up longitudinally using a diamond cutting disk from Accutom-50. The resulting cross sections were polished. Then the FEI Helios G4 CX focused ion beam (FIB) was used to cut out thin [010] TEM foils. In order to remove FIB beam damage, the specimens were ion polished for several hours using a low energy Fischione NanoMill system. STEM microscopy was then performed using a Tecnai Supertwin F20 operating in the scanning transmission electron microscopy (STEM) mode and using an annular dark field detector, as described by Jácome et al. [57].

### 3. Results

#### 3.1. Microstructural evolution during uniaxial creep testing

We first consider the evolution of microstructure during

uniaxial [001] creep testing (FUMTC specimens). Fig. 4 shows four SEM micrographs which illustrate the evolution of the  $\gamma/\gamma'$ -microstructure during uniaxial tensile creep. All SEM micrographs were taken from dendritic regions in the center of the uniaxial creep specimens. Fig. 4a shows the microstructure of the initial state prior to creep. After 81 h of creep exposure (accumulated uniaxial strain:  $\epsilon = 0.9\%$ ) the microstructure has already fully rafted, Fig. 4b. Longer creep exposures result in coarsening of the rafted microstructure (Fig. 4c: 169 h, 1.6%; Fig. 4d: 306 h, 23.3%). In Fig. 4d the  $\gamma'$ -phase is the continuous phase and the  $\gamma$ -phase has started to form isolated islands. The results of the quantitative metallographic evaluation of this microstructural evolution are presented in Fig. 5. The black point in the schematic image of the FUMTC specimen indicates the location where the metallographic measurements were performed. Fig. 5a shows that the  $\gamma$ -channel widths increase with the increase of creep exposure. The  $\gamma'$ -particles sizes in loading direction decrease first, reach a minimum and then start to increase again, Fig. 5b. Fig. 5c shows that the two procedures which were used to evaluate the  $\gamma'$ -volume fractions show the same trends but do not yield identical values. For reference the thermodynamic equilibrium value calculated by Yardley et al. [52] is shown as a horizontal dashed line. Fig. 5c shows that the volume fraction obtained from the projected area fractions is in better agreement with the thermodynamic predictions than the volume fraction which was obtained evaluating line segments. Finally, Fig. 5d shows how the  $R$ -values increase as the microstructure evolves towards topological inversion.

#### 3.2. Microstructural evolution in circular notched miniature creep specimens

The microstructural evolution measured in the center of CNMTC specimens are shown in Fig. 6. For comparison the microstructural trends observed during FUMTC testing in Fig. 4 are shown as dashed lines. All measurements were performed in D regions and are plotted as a function of square root of time. It can be seen that the evolution of the  $\gamma/\gamma'$ -microstructure in the center of the CNMTC specimens is delayed as compared to that observed in FUMTC

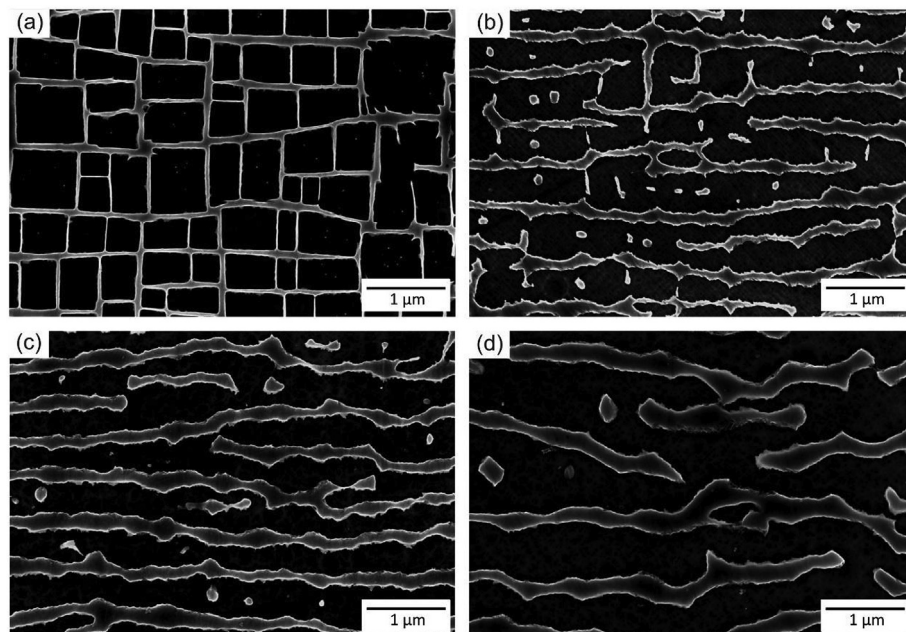


**Fig. 4.** SEM micrographs showing the evolution of the  $\gamma/\gamma'$ -microstructure during uniaxial [001] tensile creep of ERBO1 at 950 °C and 300 MPa. (a) Initial state prior to creep. (b) 81 h creep exposure ( $\epsilon = 0.9\%$ ). (c) 169 h creep exposure ( $\epsilon = 1.6\%$ ). (d) 306 h creep exposure ( $\epsilon = 23.3\%$ ).

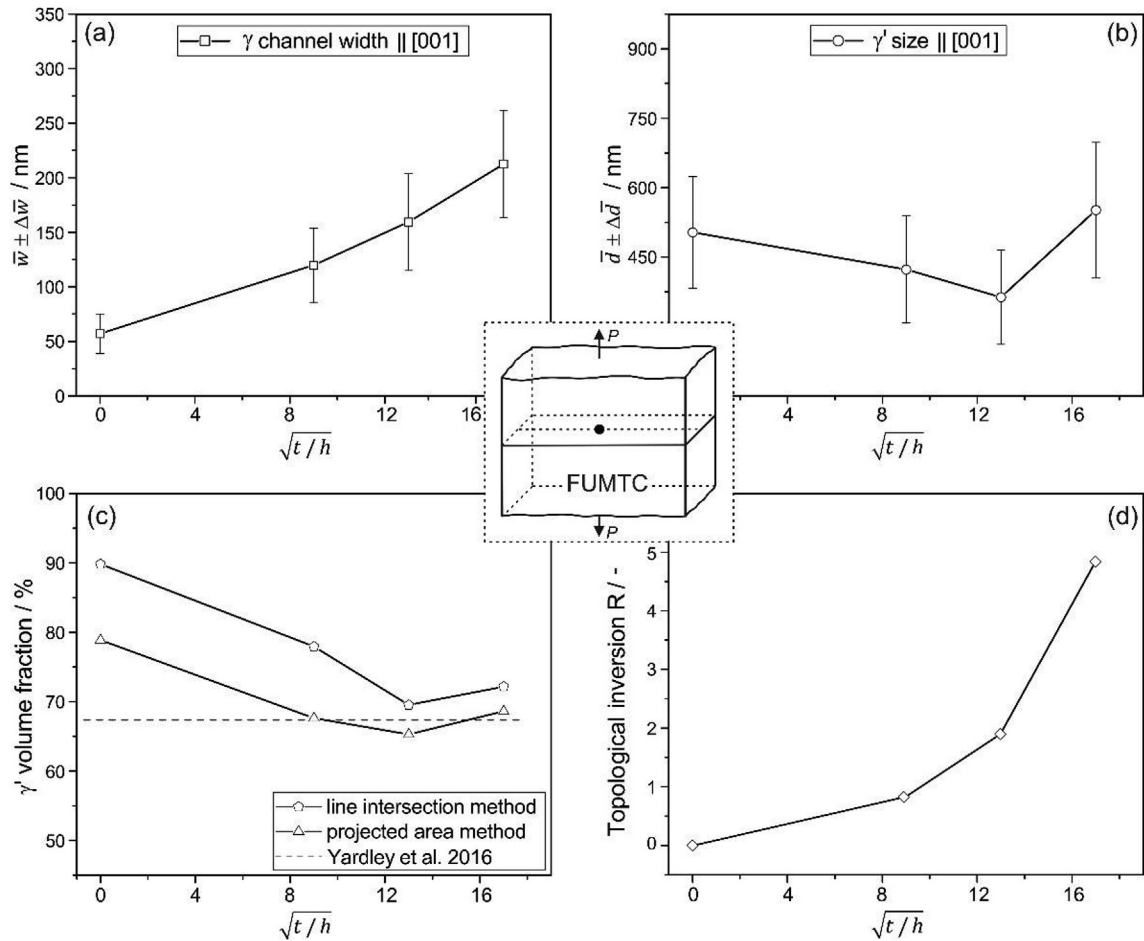


**Fig. 5.** Evolution of microstructural parameters during uniaxial [001] tensile testing. All parameters are plotted as a function of the square root of the creep exposure time. (a)  $\gamma$ -channel width measured in loading direction  $\bar{w} \pm \Delta w$ . (b)  $\gamma'$ -size measured in loading direction  $\bar{d} \pm \Delta d$ . (c)  $\gamma'$ -volume fraction (line intersection method and projected area method). (d) Parameter  $R$  (Epishin-method [19]).

specimens. No microstructural changes were detected in the center of the CNMTC specimens up to a creep exposure time of 169 h. However, after 306 h, the microstructural parameters evolved towards the values observed in FUMTC specimens.

The SEM micrographs in Fig. 7 were taken from CNMTC specimens after 169 and 306 h of creep exposure at three positions in the notch root cross section (positions 1, 2, and 3 as defined in Fig. 2a). It can be clearly seen that after 169 h of creep, microstructures at the three positions of the CNMTC specimen are very different. In the center of the CNMTC specimen (position 1), one can hardly detect any microstructural change (top SEM micrograph of left column of SEM micrographs in Fig. 7a). In contrast, close to the notch root (position 3) the microstructure has fully rafted (bottom SEM micrograph in Fig. 7a). The microstructural evolution at position 2 has reached a stage which lies in between those observed at positions 1 and 3 (middle SEM micrograph in Fig. 7a). These fascinating differences fade away during longer term creep exposures, shown in Fig. 7b.

Fig. 8 summarizes results on microstructural evolution that occurs during creep of CNMTC and FUMTC specimens. The positions of the four locations analyzed are given in the 3D schematic of CNMTC specimens in Fig. 8a. Fig. 8b shows the results obtained for the  $\gamma$ -channel widths  $\bar{w} \pm \Delta w$  (presented on y-axis of Fig. 8b) at locations 1, 2, and 3 (assigned to x-axis). The two dashed lines connect the data points which correspond to the 81 h (lower rising dashed line) and 306 h (upper horizontal dashed line) creep

exposure times. The two vertical arrows point upwards indicating an increase of creep exposure time from 81 h (full black symbols) to 306 h (full blue triangles). Fig. 8b shows that for long enough creep exposure times the  $\gamma$ -channel widths reach a saturation value which no longer depends on the position of the investigated microstructure in the cross section of the CNMTC specimen. Fig. 8c shows the values of  $\gamma'$ -volume fractions measured with projected area method at positions 1, 2 and 3 after 169 and 306 h of creep exposure.

Fig. 8c also shows a dashed horizontal line, which indicates the thermodynamic equilibrium value expected for the alloy composition considered (see Yardley et al. [52]). Fig. 8c clearly shows that after 169 h of creep exposure the microstructure still evolves towards a new equilibrium volume fraction. The kinetics of this process differs for different locations in the CNMTC specimen. After 306 h of creep exposure, the new equilibrium value is reached everywhere in the notch root cross section of the CNMTC specimen. In Fig. 8d the x-axis no longer represents numbered locations in the CNMTC specimen. Instead the  $R$  values which quantify topological inversion at positions 1, 2, 3 and 4 in the CNMTC specimen and in the center of a FUMTC specimen are plotted as function of square root of time. Topological inversion occurs rapidly in the FUMTC specimen (black squares in Fig. 8d). Fig. 8d also clearly shows that the evolution of  $R$  in the notch root (position 3) is very similar to the evolution during uniaxial testing. From the data at position 2 we observed a similar trend, although the evolution was slower than at

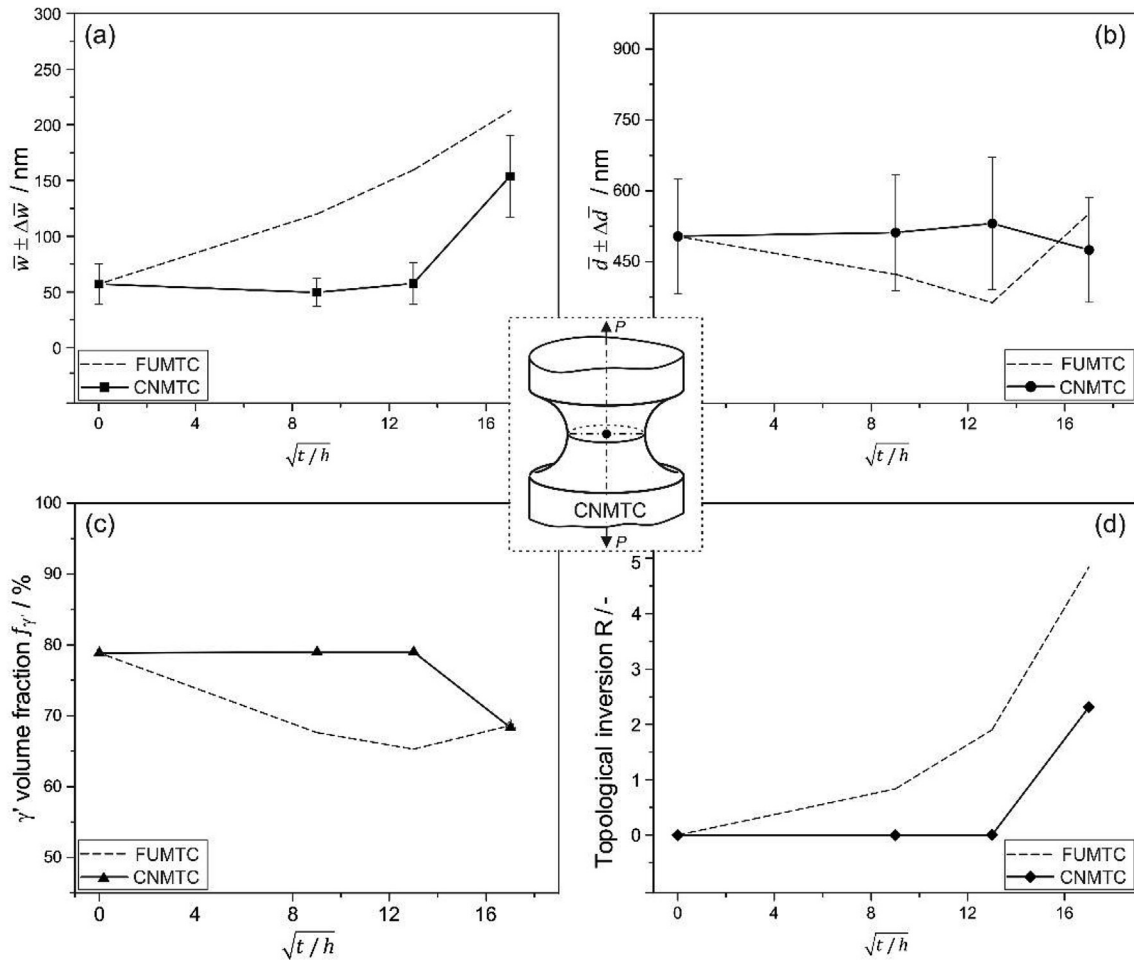


**Fig. 6.** Comparison of the microstructural characteristics in FUMTC and CNMTC  $\langle 100 \rangle$  specimens after creep at 950 °C and net section stress of 300 MPa. (a)  $\gamma$ -channel width  $\bar{w} \pm \Delta w$ . (b)  $\gamma'$ -size  $\bar{d} \pm \Delta d$ . (c)  $\gamma'$ -volume fraction (results from projected area method). (d) Topological inversion parameter  $R$ .

position 3. However, it took a much longer time at position 1 for the  $R$  value to follow the same trend. At position 4 in the CNMTC specimen no topological inversion was observed (SEM images not shown in the present work).

Fig. 9 shows the STEM micrographs which were obtained in the centers (positions 1) and the notch roots (positions 3) of the specimens which were creep exposed for 169 and 306 h. The quality of the images suffer from some remaining FIB beam damage, but the  $\gamma/\gamma'$ -microstructures and the dislocation substructures can be well distinguished. A comparison between Fig. 9a and Fig. 9b shows that after 169 h the center of the specimen is barely affected by creep (absence of rafting, low dislocation density). The notch root of the 169 h specimen, in contrast, shows a  $\gamma/\gamma'$ -microstructure which has already rafted and exhibits a high dislocation density in the  $\gamma$ -channels. After 306 h, it is difficult to find significant differences between the center and the notch root of the specimen. At both locations, the  $\gamma/\gamma'$ -microstructures are fully rafted and dislocation densities are high.

## 4. Discussion

### 4.1. Importance of choice of test procedure and creep parameters

The experimental approach used in the present work has a few advantages when compared to most previous studies. First, our miniature SX specimens can be precisely oriented [50,53]. Agudo

Jácóme et al. [27,28] documented that when a negative misfit Ni-base SX is subjected to  $\langle 110 \rangle$  tensile creep in the high temperature low stress creep regime, rafting occurs in two equivalent  $45^\circ$  directions (see Fig. 9e in Ref. [27] and Fig. 7 in Ref. [28]). Tian et al. [58] also performed  $\langle 110 \rangle$  creep tests on a Ni-base SX. Their specimen was only slightly misoriented ( $4^\circ$  off of the precise  $\langle 110 \rangle$  direction). As a result, they observed rafting in only one  $45^\circ$  direction. Second, the quantitative SEM metallographic measurements of the present study were exclusively performed in prior dendritic regions because the  $\gamma'$ -volume fractions between prior D and ID regions can differ [51]. For the alloy investigated in the present work it was found experimentally that the  $\gamma'$ -volume fractions in D and ID regions of the as-received material were 72% and 77%, respectively [51]. This was later confirmed by thermodynamic calculations based on the local chemical compositions in D and ID regions [52]. Third, there is a strong technological interest in long term creep data and creep experiments are often designed with this in mind. For the type of parametric fundamental study performed in the present work, tests have to be performed in a stress and temperature range, where stress redistribution in notched specimens is not too fast and microstructures evolve in laboratory time scales (i.e.  $< 500$  h). The conditions used in the present work, 950 °C and 300 MPa and exposure times of 81, 169 and 306 h fulfill this requirement. Experimental studies at temperatures well above 1000 °C as performed for CMSX-4 in Ref. [36] suffer from the drawback that the evolution of the microstructure is

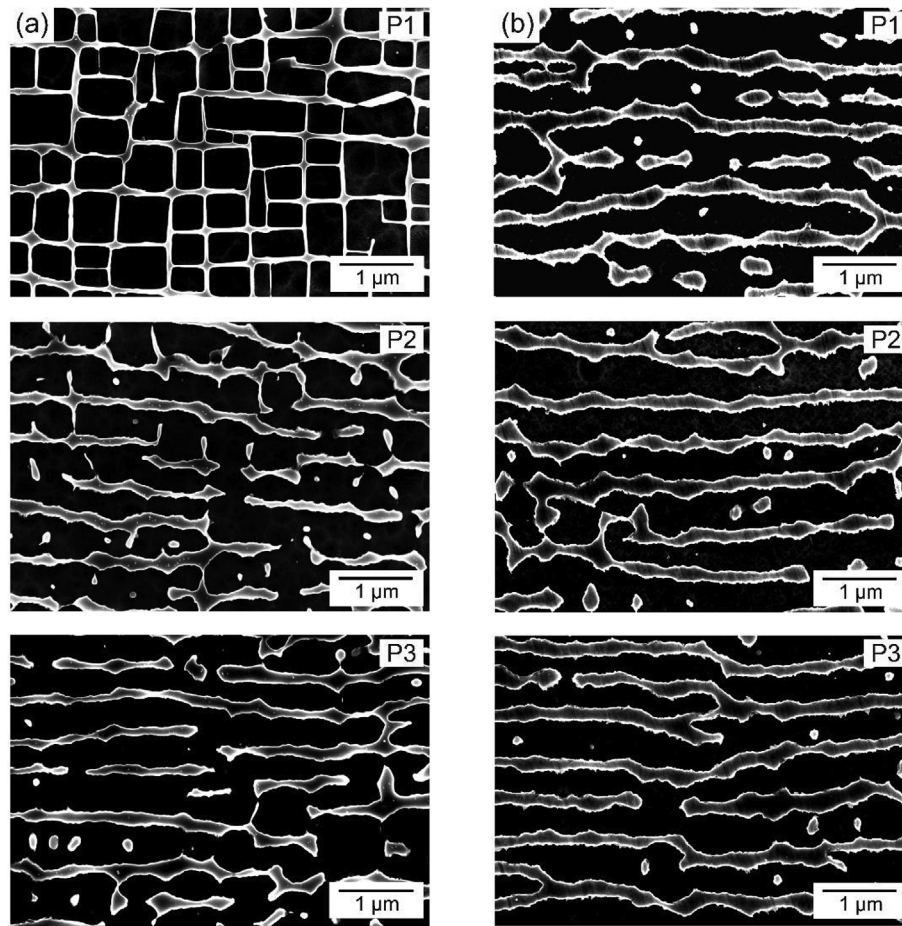


**Fig. 7.** SEM micrographs showing the microstructures at different radial positions after CNMTC creep (950 °C, net section stress 300 MPa). (a) Left column of SEM micrographs: Creep exposure time 169 h. (b) Right column of SEM micrographs: Creep exposure time 306 h.

strongly affected by the dissolution of the  $\gamma'$ -phase [30]. An increasing  $\gamma$ -channel width may be simply associated with the dissolution of the  $\gamma'$ -phase. Fedelich et al. [17,18] investigated a CMSX-4 specimen with a mild notch at 950 °C, and a net section stress of 180 MPa. They did not detect any rafting after 700 h of creep, even though they reported that under this creep condition rafting was a prominent feature in uniaxial tests. Rafting occurred when the stress and exposure time were slightly raised to 200 MPa and 1000 h [17,18]. Fourth, confidence in the quantitative metallographic data increases when the experimental volume fractions established after sufficiently long exposure time agree with thermodynamic predictions [52], as is shown in Fig. 5c. The advantages of the test procedure described in this section outweigh the disadvantages which are associated with the miniature test technique and the test parameters which were chosen: microstructural scatter has a stronger influence on mechanical properties, it is more difficult to measure strain, and the duration of the experiments is short as compared to the anticipated service life of high temperature components.

#### 4.2. Quantification of microstructural evolution

All elementary processes which control the evolution of the microstructural parameters shown in Figs. 5 and 6 are diffusion controlled. This is why the evolution of  $\gamma$ -channel widths  $w$ ,  $\gamma'$ -particle sizes  $d$ ,  $\gamma'$ -volume fractions  $f_{\gamma'}$  and the inversion parameter  $R$  are plotted as a function of square root of time. The observed

increase of the  $\gamma$ -channel width (Fig. 5a), a parameter which is known to show a high microstructural scatter [17,59], is in agreement with what has been reported by other authors under uniaxial and multiaxial test conditions [17,28,36]. The early decrease of  $\gamma'$ -sizes in Fig. 5b is partly related to the fact that the overall  $\gamma'$ -volume fraction decreases as the material establishes a new equilibrium at creep temperature and to the fact that  $\gamma'$ -material is needed to close the vertical  $\gamma$ -channels (for a detailed discussion see Ref. [30]). This early decrease in  $\gamma'$ -size is not seen in Fig. 6b (notched specimen) where it probably manifests itself after 169 and before 306 h. In both types of tests, the volume fractions of the  $\gamma'$ -phase decrease during creep, towards the 950 °C thermodynamic equilibrium calculated using MatCalc [52] based on the local chemical composition of the dendritic region as reported in Ref. [51]. Fig. 5c shows that a line intersection method can be used to identify trends in the evolution of the volume fraction of the  $\gamma'$ -phase. However, the volume fractions derived from the projected area fractions of the  $\gamma'$ -phase yield results which are closer to the thermodynamic prediction, Fig. 5c. Therefore, in Fig. 6c only this volume fraction is used and the results of the line intersection method are no longer considered. In both types of specimens the topological inversion parameter  $R$  [23] increases throughout creep, as shown in Figs. 5d and 6d.

#### 4.3. On threshold stresses for rafting and on the delay of microstructural evolution in the center of notched specimens

The results of the present work show that even after 306 h of

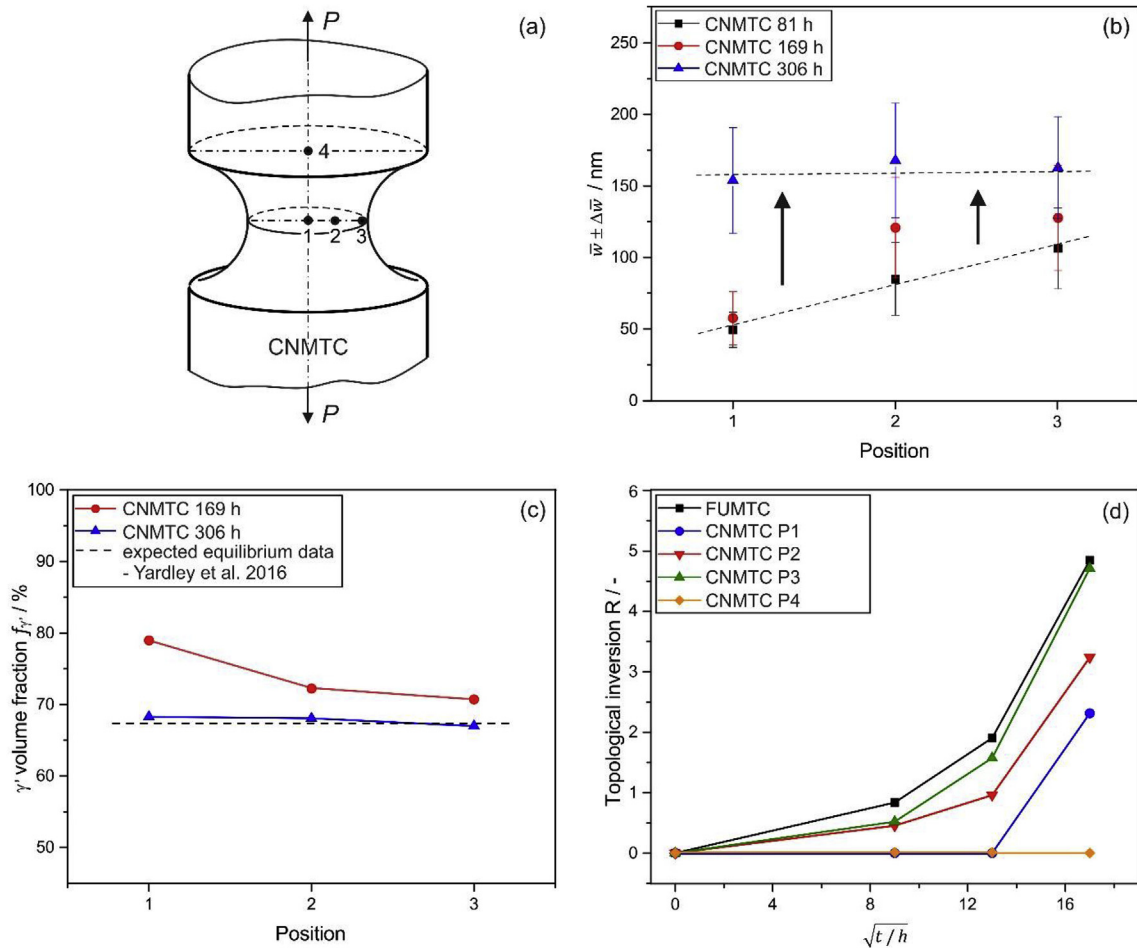


**Fig. 8.** Overview summary of microstructural results obtained from interrupted creep tests with CNMTC and FUMTC specimens. (a) Locations of analysis in CNMTC specimen. (b)  $\gamma'$ -channel width  $\bar{w} \pm \Delta \bar{w}$  (y-axis) at positions 1, 2 and 3 (x-axis). Three data sets for 81, 169 and 306 h of creep exposure are shown. (c)  $\gamma'$ -volume fraction from projected area method (y-axis) at positions 1, 2 and 3 after 169 and 306 h of creep exposure. The dashed horizontal line shows the expected equilibrium data calculated by Yardley et al., (2016). (d) Evolution of the topological inversion parameter  $R$  as a function of square root of time. Comparison of different locations in CNMTC specimen with results from FUMTC specimen. For details see text.

creep, no rafting was observed at position 4 (Fig. 2a) of the circular notched specimen, where the tensile stress is 75 MPa (SEM images not shown). This indicates that at a given temperature, a minimum stress level is required for rafting to occur. A comparison between the microstructural results obtained in uniaxial (FUMTC) and circular notched (CNMTC) specimens shows that the presence of a mild circular notch significantly delays microstructural evolution. Microstructural evolution in the center of the circular notched specimen is hampered due to the low axial stress  $\sigma_L$  in loading direction in the early stages of creep. We find that rafting in the center of the specimen can only proceed when the stress redistribution has established a sufficiently high axial stress  $\sigma_L$ , Fig. 1b. The fact that microstructural evolution is suppressed in the presence of a circular notch is also in line with the results reported by Fedelich et al. [17]. They report that no rafting is observed in a mild V-notched specimen subjected to creep at 950 °C and 180 MPa net section stress, while it does occur under the same conditions of stress and temperature in the absence of a notch. Fedelich et al. [18] documented a microstructural scenario after 1000 h creep at 950 °C and 200 MPa, where no rafting has occurred in the center of the notched specimen while a fully rafted microstructure has evolved in the notch root. This result corresponds to the findings we report in Fig. 7a.

#### 4.4. Microstructural evolution from rafting to topological inversion

It has been shown that extremely small secondary  $\gamma'$ -particles ( $d < 20$  nm) have spherical shapes and that they start to take on cuboidal geometries when they grow ( $d > 20$  nm) [52]. There is a competition between the tendency to minimize surface energy (which dominates for small particle sizes and increases with particle size) and the tendency to keep the overall strain energy (which increases with particle size) as small as possible [64]. The growth of the elastic strain energy with particle size is stronger than the increase of surface energy. Therefore, elastic strain energy criteria can be successfully used to predict particle shapes [7,13]. They take into account that the elastic modulus shows minima in  $\langle 100 \rangle$  directions (see recent data published by Demtröder et al. [60]). There is a general agreement that rafting, the directional coarsening of the  $\gamma'$ -phase during  $\langle 100 \rangle$  tensile testing of negative misfit Ni-base superalloys, is governed by the tendency to minimize overall strain energy. But one must then ask the question why topological inversion occurs in the later stages of creep [23]. Why is there no more need to minimize stress components by creating  $\{100\}$  type of interfaces? Our results show that the parameter  $R$  which quantifies this microstructural phenomenon increases throughout uniaxial creep, and, with a delay, also in the later stages of creep in the center of circular notched specimens, Figs. 5d, 6d

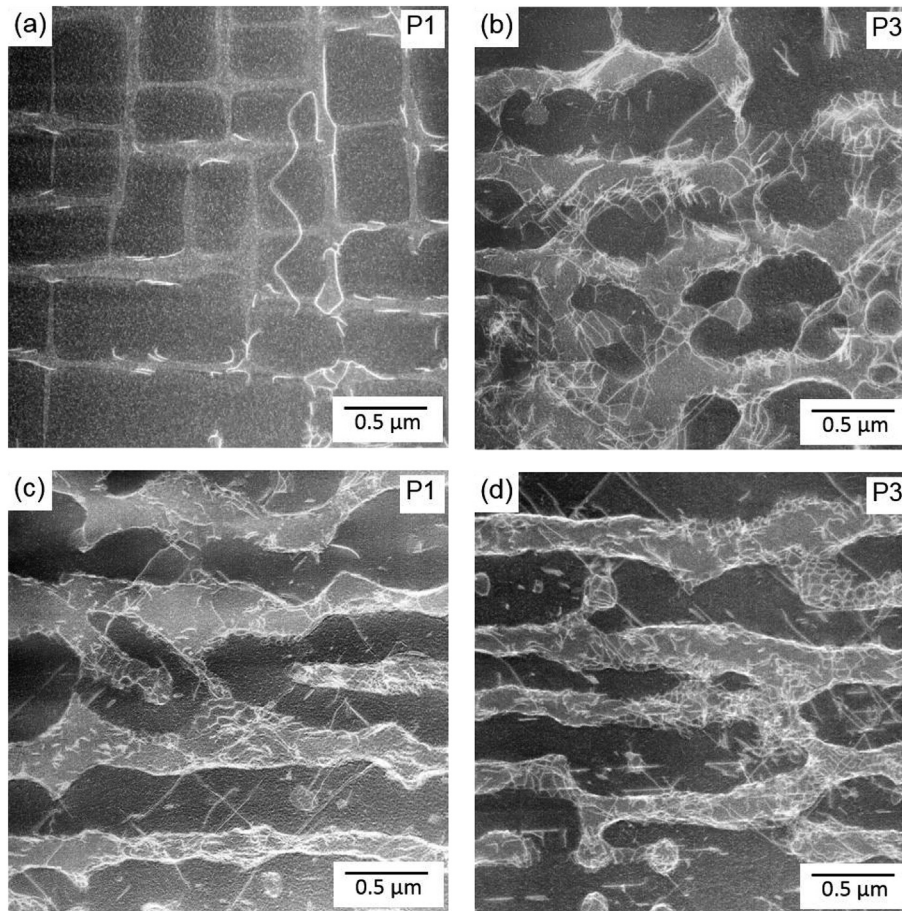


**Fig. 9.** STEM images taken from positions 1 and 3 of CNMTC specimens after 169 h and 306 h of creep. (a) 169 h CNMTC specimen: position 1. (b) 169 h CNMTC specimen: position 3. (c) 306 h CNMTC specimen: position 1. (d) 306 h CNMTC specimen: position 3.

and 8d. In all cases the microstructure evolves towards this morphology which has also been observed by Caccuri et al. [36] under multiaxial test conditions. We suggest that this is due to the fact that as the dislocation density in the  $\gamma$ -channels increases in the early stages of creep, their stress fields accommodate the stress fields associated with the crystallographic misfit between the  $\gamma$ - and the  $\gamma'$ -phase. This can be described as

$$\sigma_M + \sigma_{\text{disl}} = 0 \quad (7)$$

where  $\sigma_M$  is the contribution of the coherency stress fields associated with lattice misfit and  $\sigma_{\text{disl}}$  stands for the stress fields of the dislocations. Therefore, when the microstructural evolution has led to the formation of rafts which are covered by misfit dislocation networks [61], the system switches from minimizing elastic strain energy to minimizing internal interfacial energies. STEM micrographs from the Ni-base SX alloy investigated in the present work (e.g. Fig. 13c from Ref. [53]) and in other studies (e.g. Fig. 5 of [28]) show isolated  $\gamma$ -regions which have evolved during low temperature and high stress creep support this view. Further work is required to understand this part of microstructural evolution during creep, because it may well contribute to an increase in creep rates during tertiary creep [23,62,63].

#### 4.5. Microstructural evolution under redistributing stresses and the effect of stress multiaxiality

As a striking new result we find that there is a correlation

between stress redistribution and microstructural evolution during creep in circular notched tensile creep specimens, as outlined in Section 4.3 and shown in Fig. 7. It should be pointed out that higher axial local stresses are associated with higher axial strains. One can also use the argument of Matan et al. [22]: after 169 h, strains have surpassed the critical threshold strain in the notch root but not yet in the center of the notch root cross section. Later, after stress redistribution, this critical threshold strain is also established in the center of the notched specimen. During high temperature and low stress creep, the rafts form perpendicular to loading direction under uniaxial  $\langle 100 \rangle$  loading [3,53]. In the macroscopic crystallographic shear system  $\langle 1-10 \rangle \{110\}$  rafts form in  $45^\circ$  to the direction of shear loading and perpendicular to the direction of the maximum principal stress [24,29]. These results support the view that the maximum principal stress is the key component of the overall stress state which governs rafting.

The recent work of Caccuri et al. [36] is the only other study performed so far, which tackles local microstructural evolution in a specimen where stress states evolve during creep. They investigate CMSX-4 at  $1093^\circ\text{C}$  and a net section stress close to 90 MPa. Their specimen is not a symmetric circular notched specimen. Instead it was made from a long flat piece (width: 6 mm, thickness: 0.75 mm) which contained a V-shaped section. During testing, this produces an inhomogeneous stress state which evolves from tensile to compressive. This allows to investigate the influence of positive and negative as well as of low and high stress triaxialities. One of their conclusions is that the  $\gamma'$  raft orientation correlates well with stress

triaxiality. While this holds for their experimental results, the results obtained in the present work show that after sufficiently long creep times, rafts look the same, no matter whether the stress triaxialities are low (notch root) or high (center), Fig. 1d. The present work and the study of Caccuri et al. [36] have two aspects in common. First, that the rafting process follows the kinetics of the stress redistribution during creep. Second, at the end all  $\gamma/\gamma'$ -microstructure evolve towards a topologically inverted microstructure. Yue and co-workers [30,31] investigated a similar SX superalloy with a lower Re content than the material used in the present work. They used a higher test temperature of 980 °C, a higher net section stress of 400 MPa and considered a sharp notch. Yue et al. [33–35] also combined experimental work with finite element creep stress analysis and showed that the features of rafting in tensile specimens oriented in  $\langle 100 \rangle$ ,  $\langle 110 \rangle$  and  $\langle 111 \rangle$  directions depend on the position of the microstructural region relative to the position of a sharp V-notch. They did not consider the evolution of the raft microstructure with time and the focus of their work is on the evolution of porosity, micro crack damage and notch root cracking.

#### 4.6. On the effect of stress state on rafting

The results obtained in the present work is another example showing the fact that rafting reacts sensitively to different stress states. As far as local internal stress states are concerned, the raft morphology has been shown to be affected by elevated dislocation densities next to a hardness indent [20], by solidification stresses associated with differences between prior dendritic and interdendritic regions [37,38] and by stress concentrations next to pores [64]. In the case of complex specimen geometries where loading results in non-homogeneous macroscopic stress states, the raft morphology is governed by these stress states [17,18,24,29,31,32,34–36,65,66]. It is well appreciated that a local stress state  $\sigma_{loc}$  in the microstructure of a Ni-base SX superalloy results from a superposition of different stress components [67].

$$\sigma_{loc} = \sigma_{ext} + \sigma_M + \sigma_{disl} \quad (8)$$

where  $\sigma_{ext}$  represents the stress state associated with external loading.

The fact that Caccuri et al. [36] observed that microstructure evolves faster towards topological inversion under compressive (negative stress triaxialities) than under tensile type of stress states is probably related to the fact, that the compressive external stresses can accommodate misfit stresses, which makes it easier for the  $\gamma'$ -phase to form.

## 5. Summary and conclusions

The present work compares the evolution of  $\gamma/\gamma'$ -microstructures and dislocation densities during high temperature (950 °C) and low stress creep in flat uniaxial miniature tensile creep specimens (FUMTC, uniaxial stress: 300 MPa) and circular notched miniature tensile creep specimens (CNMTC, net section stress: 300 MPa) loaded in precise [001] directions. All mechanical details on the CNMTC specimen were recently given by Cao et al. [50]. Electron microscopy (SEM and STEM) were used in prior dendritic regions of the microstructure to characterize the evolution of the  $\gamma/\gamma'$ -microstructure and of the dislocation substructure. For both types of tensile tests, experiments were interrupted after 81, 169, and 306 h. From the results obtained in the present work the following conclusions can be drawn:

During [001] uniaxial tensile creep, the microstructure evolves homogeneously in the whole specimen cross section. The kinetics

of  $\gamma$ -channel widening follows a parabolic rate law, which suggests that the evolution of the microstructure occurs diffusion controlled. The microstructure evolves from rafting towards topological inversion, indicating that while the early stages of rafting are governed by a driving force related to mechanical anisotropies resulting from a superposition of misfit and external stress components, the later stages, where misfit dislocation networks accommodate elastic misfit stresses, are dominated by the overall tendency to minimize interfacial energy. This finally leads to topological inversion and suggests that rafting only represents an intermediate state of microstructural evolution.

As a striking new result it was found that microstructural evolution in the circular notched specimen is coupled to the kinetics of stress redistribution during creep. Rafting (studied by SEM), the directional coarsening of the  $\gamma'$ -phase, and the increase of dislocation density (studied by STEM) start in the notch root before the center of the specimen is affected. When stresses in the circular notched specimens are fully redistributed, there are no more differences in terms of  $\gamma/\gamma'$ -microstructure and dislocation densities between the notch root and the center of the circular notched specimen.

The results obtained in the present work suggest that the maximum principal stress is more important than stress triaxiality in affecting the nature of rafting. After sufficiently long times of creep exposure of circular notched specimens, rafts form homogeneously over the notch root cross section, no matter whether the stress triaxiality is low (notch root) or high (center). Moreover, the results support the view that strain accumulation coupled to an increase of overall dislocation density is important in rafting.

## Acknowledgements

All authors acknowledge funding through project A1 of the collaborative research center SFB/TR 103 on superalloy single crystals. L. Cao acknowledges funding from the China Scholarship Council (File No. 201406830001) and support from the International Max Planck Research School SurMat.

## References

- [1] M. Durand-Charre, *The Microstructure of Superalloys*, CRC Press, Boca Raton, 1997.
- [2] M.J. Donachie, S.J. Donachie, *Superalloys: a Technical Guide*, ASM International, Materials Park, Ohio, 2002.
- [3] R.C. Reed, *The Superalloys: Fundamentals and Applications*, Cambridge university press, Cambridge, 2006.
- [4] B. Geddes, H. Leon, X. Huang, *Superalloys: Alloying and Performance*, ASM International, Materials Park, Ohio, 2010.
- [5] J.K. Tien, S.M. Copley, The effect of uniaxial stress on the periodic morphology of coherent gamma prime precipitates in nickel-base superalloy crystals, *Metall. Trans. 2* (1971) 215–219.
- [6] J.K. Tien, S.M. Copley, The effect of orientation and sense of applied uniaxial stress on the morphology of coherent gamma prime precipitates in stress annealed nickel-base superalloy crystals, *Metall. Trans. 2* (1971) 543–553.
- [7] A. Pineau, Influence of uniaxial stress on the morphology of coherent precipitates during coarsening-elastic energy consideration, *Acta Metall.* 24 (1976) 559–564.
- [8] W.C. Johnson, T.A. Abinandanan, P.W. Voorhees, The coarsening kinetics of two misfitting particles in an anisotropic crystal, *Acta Metall. Mater.* 38 (1990) 1349–1367.
- [9] S. Socrate, D.M. Parks, Numerical determination of the elastic driving force for directional coarsening in Ni-superalloys, *Acta Metall. Mater.* 41 (1993) 2185–2209.
- [10] F.R.N. Nabarro, Rafting in superalloys, *Metall. Mater. Trans.* 27 (1996) 513–530.
- [11] F.R.N. Nabarro, C.M. Cress, P. Kotschy, The thermodynamic driving force for rafting in superalloys, *Acta Mater.* 44 (1996) 3189–3198.
- [12] M. Véron, Y. Bréchet, F. Louchet, Directional coarsening of Ni-based superalloys: computer simulation at the mesoscopic level, *Acta Mater.* 44 (1996) 3633–3641.
- [13] D.J. Arrell, J.L. Vallés, Rafting prediction criterion for superalloys under a multiaxial stress, *Scripta Mater.* 35 (1996) 727–732.

- [14] M.P. Gururajan, T.A. Abinandanan, Phase field study of precipitate rafting under a uniaxial stress, *Acta Mater.* 55 (2007) 5015–5026.
- [15] A. Gaubert, Y. Le Bouar, A. Finel, Coupling phase field and viscoplasticity to study rafting in Ni-based super alloys, *Philos. Mag* 90 (2010) 375–404.
- [16] N. Zhou, C. Shen, M. Mills, Y. Wang, Large-scale three-dimensional phase field simulation of  $\gamma'$ -rafting and creep deformation, *Philos. Mag* 90 (2010) 405–436.
- [17] B. Fedelich, A. Epishin, T. Link, H. Klingelhöffer, G. Künecke, P.D. Portella, Experimental characterization and mechanical modeling of creep induced rafting in super alloys, *Comput. Mater. Sci.* 64 (2012) 2–6.
- [18] B. Fedelich, A. Epishin, T. Link, H. Klingelhöffer, G. Künecke, P.D. Portella, Rafting during high temperature deformation in a single crystal superalloy, in: S. Huron, et al. (Eds.), *Superalloys 2012*, Proc. Of the 12th International Symposium on Superalloys, TMS, Warrendale, 2012, pp. 491–500.
- [19] T.M. Pollock, A.S. Argon, Directional coarsening in nickel-base single crystals with high volume fractions of coherent precipitates, *Acta Metall.* 42 (1994) 1859–1874.
- [20] M. Véron, Y. Bréchet, F. Louchet, Strain induced directional coarsening in Ni based super alloys, *Scripta Mater.* 34 (1996) 1883–1886.
- [21] M. Véron, P. Bastie, Strain induced directional coarsening in nickel based superalloys: investigation on kinetics using the small angle neutron scattering (SANS) technique, *Acta Mater.* 45 (2015) 3277–3282.
- [22] N. Matan, D.C. Cox, C.M.F. Rae, R.C. Reed, On the kinetics of rafting in CMSX-4 superalloy single crystals, *Acta Mater.* 47 (1999) 2031–2045.
- [23] A. Epishin, T. Link, U. Brückner, P. Portella, Kinetics of the topological inversion of the  $\gamma/\gamma'$ -microstructure during creep of a nickel-based superalloy, *Acta Mater.* 49 (2001) 4017–4023.
- [24] M. Kamaraj, Rafting in single crystal nickel-base super alloys – an overview, *Sadhana Acad. Proc. Eng. Sci.* 28 (2003) 115–128.
- [25] R.C. Reed, D.C. Cox, C.M.F. Rae, Kinetics of rafting in a single crystal superalloy: effects of residual microsegregation, *Mater. Sci. Technol.* 23 (2007) 893–902.
- [26] X. Milhet, M. Arnoux, J. Cormier, J. Mendez, C. Trosas, On the influence of the dendritic structure on the creep behavior of a Re-containing superalloy at high temperature/low stress, *Mater. Sci. Eng., A* 546 (2012) 139–145.
- [27] L. Agudo Jácome, P. Nörtershäuser, J.-K. Heyer, A. Lahni, J. Frenzel, A. Dlouhy, C. Somsen, G. Eggeler, High-temperature and low-stress creep anisotropy of single-crystal super alloys, *Acta Mater.* 61 (2013) 2926–2943.
- [28] L. Agudo Jácome, P. Nörtershäuser, C. Somsen, A. Dlouhy, G. Eggeler, On the nature of  $\gamma'$  phase cutting and its effect on high temperature and low stress creep anisotropy of Ni-base single crystal super alloys, *Acta Mater.* 69 (2014) 246–264.
- [29] M. Kamaraj, C. Mayr, M. Kolbe, G. Eggeler, On the influence of stress state on rafting in the single crystal superalloy CMSX-6 under conditions of high temperature and low stress creep, *Scripta Mater.* 38 (1998) 589–594.
- [30] K. Serin, G. Göbenli, G. Eggeler, On the influence of stress state, stress level and temperature on  $\gamma$ -channel widening in the single crystal superalloy CMSX-4, *Mater. Sci. Eng.* 387–389 (2004) 133–137.
- [31] H. Tamaki, K. Fujita, A. Okayama, N. Matsuda, Y. Yoshinari, K. Takeki, A study on bending deformation behavior of Ni-based DS and SC super alloys, in: K.A. Green, et al. (Eds.), *Superalloys 2004*, TMS, Seven Springs, 2004, pp. 145–154.
- [32] P. Wollgramm, P. Nörtershäuser, G. Eggeler, On the coarsening of the  $\gamma/\gamma'$ -microstructure in crack tip stress fields of differently oriented single crystalline miniature CT-specimens at 1020 °C, in: Proc. 12th Int. Conf. Creep and Fracture of Engineering Materials and Structures (JIMIS 11), Kyoto, Japan, 2012, A09.
- [33] D.S. Liu, D.X. Zhang, J.W. Liang, Z.X. Wen, Z.F. Yue, Prediction of creep rupture life of a V-notched bar in DD6 Ni-based single crystal superalloy, *Mater. Sci. Eng., A* 615 (2014) 14–21.
- [34] D. Liu, Z. Wen, Z. Yue, Creep damage mechanism and  $\gamma'$ -phase morphology of a V-notched round bar in Ni-based single crystal superalloys, *Mater. Sci. Eng., A* 605 (2014) 215–221.
- [35] Z. Wen, D. Zhang, S. Li, Z. Yue, J. Gao, Anisotropic creep damage and fracture mechanism of nickel-base single crystal superalloy under multiaxial stress, *J. Alloy. Comp.* 692 (2017) 301–312.
- [36] V. Caccuri, J. Cormier, R. Desmorat,  $\gamma'$ -Rafting mechanisms under complex mechanical stress state in Ni-based single crystalline superalloys, *Mater. Des.* 131 (2017) 487–497.
- [37] A. Hazotte, J. Lacaze, Chemically Oriented Gamma Prime Plate Development in a Nickel Base Superalloy, vol. 23, 1989, pp. 1877–1882.
- [38] P. Nörtershäuser, J. Frenzel, A. Ludwig, K. Neuking, G. Eggeler, The effect of cast microstructure and crystallography on rafting, dislocation plasticity and creep anisotropy of single crystal Ni-base superalloys, *Mater. Sci. Eng., A* 626 (2015) 305–312.
- [39] J. Coakley, E.A. Lass, D. Ma, M. Frost, D.N. Seidman, D.C. Dunand, H.J. Stone, Rafting and elastoplastic deformation of superalloys studied by neutron diffraction, *Scripta Mater.* 134 (2017) 110–114.
- [40] J. Coakley, D. Ma, M. Frost, D. Dye, D.N. Seidman, D.C. Dunand, H.J. Stone, Lattice strain evolution and load partitioning during creep of a Ni-based superalloy single crystal with rafted  $\gamma'$  microstructure, *Acta Mater.* 135 (2017) 77–87.
- [41] B. Ilshner, *Hochtemperaturplastizität*, Springer Verlag, Berlin, 1973.
- [42] J. Čadek, *Creep in Metallic Materials*, Elsevier, Amsterdam, 1988.
- [43] A.C.F. Cocks, M.F. Ashby, Intergranular fracture during power-law creep under multiaxial stresses, *Met. Sci.* 14 (1980) 395–402.
- [44] W.D. Nix, J.C. Earthman, G. Eggeler, B. Ilshner, The principal facet stress as a parameter for predicting creep rupture under multiaxial stresses, *Acta Metall.* 37 (1989) 1067–1077.
- [45] D.R. Hayhurst, F.A. Leckie, J.T. Henderson, Design of notched bars for creep-rupture testing under tri-axial stresses, *Int. J. Mech. Sci.* 19 (1977) 147–159.
- [46] D.R. Hayhurst, F.A. Leckie, C.J. Morrison, Creep rupture of notched bars, *Proc. R. Soc. London Ser. A-Mathematical Phys. Eng. Sci.* 360 (1978) 243–264.
- [47] D.R. Hayhurst, G.A. Webster, An overview on studies of stress state effects during creep of circumferentially notched bars, in: D.J. Gooch, I.M. How (Eds.), *Tech. Multiaxial Creep Test*, Springer Verlag, Netherlands, Dordrecht, 1986.
- [48] G. Eggeler, C. Wiesner, A numerical study of parameters controlling stress redistribution in circular notched specimens during creep, *J. Strain Anal. Eng. Des.* 28 (1993) 13–22.
- [49] G. Eggeler, W. Tato, P. Jemmely, B. deMestral, Creep rupture of circular notched P91-specimens: influence of heat treatment and notch geometry, *Scripta Metall. Mater.* 27 (1992) 1091–1096.
- [50] L. Cao, D. Bürger, P. Wollgramm, K. Neuking, G. Eggeler, Testing of Ni-base superalloy single crystals with circular notched miniature tensile creep (CNMTC) specimens, *Mater. Sci. Eng., A* 712 (2018) 223–231.
- [51] A.B. Parsa, P. Wollgramm, H. Buck, C. Somsen, A. Kostka, I. Povstugar, P.-P. Choi, D. Raabe, A. Dlouhy, J. Müller, E. Spiecker, K. Demtröder, J. Schreuer, K. Neuking, G. Eggeler, Advanced scale bridging microstructure analysis of single crystal Ni-Base superalloys, *Adv. Eng. Mater.* 17 (2015) 216–230.
- [52] V. Yardley, I. Povstugar, P.-P. Choi, D. Raabe, A.B. Parsa, A. Kostka, C. Somsen, A. Dlouhy, K. Neuking, E.P. George, G. Eggeler, On local phase equilibria and the appearance of nanoparticles in the microstructure of single-crystal Ni-base super alloys, *Adv. Eng. Mater.* 18 (2016) 1556–1567.
- [53] P. Wollgramm, D. Bürger, A.B. Parsa, K. Neuking, G. Eggeler, The effect of stress, temperature and loading direction on the creep behavior of Ni-base single crystal superalloy miniature tensile specimens, *Mater. A. T. High. Temp.* 33 (2016) 346–360.
- [54] H. Neuber, *Kerbspannungslehre – Theorie der Spannungskonzentration, Genaue Berechnung der Festigkeit*, second ed., Springer Verlag, Berlin, 1958.
- [55] R.E. Peterson, *Stress Concentration Factors*, Wiley, New York, 1974.
- [56] G.E. Dieter, *Mechanical Metallurgy*, McGraw-Hill, London, 1988.
- [57] L.A. Jácome, G. Eggeler, A. Dlouhy, Advanced scanning transmission stereo electron microscopy of structural and functional engineering materials, *Ultramicroscopy* 122 (2012) 48–59.
- [58] S. Tian, Y. Su, L. Yu, H. Yu, S. Zhang, B. Qian, Microstructure evolution of a [011] orientation single crystal nickel-base superalloy during tensile creep, *Appl. Phys. A Mater. Sci. Process* 104 (2011) 643–647.
- [59] X. Wu, P. Wollgramm, C. Somsen, A. Dlouhy, A. Kostka, G. Eggeler, Double minimum creep of single crystal Ni-base superalloys, *Acta Mater.* 112 (2016) 242–260, <https://doi.org/10.1016/j.actamat.2016.04.012>.
- [60] K. Demtröder, G. Eggeler, J. Schreuer, Influence of microstructure on macroscopic elastic properties and thermal expansion of nickel-base superalloys ERBO/1 and LEK94, *Mater. Werkst.* 46 (2015) 563–576, <https://doi.org/10.1002/mawe.201500406>.
- [61] M. Probst-Hein, A. Dlouhy, G. Eggeler, Interface dislocations in superalloy single crystals, *Acta Mater.* 47 (1999) 2497–2510.
- [62] P. Caron, C. Ramusat, F. Diologent, Influence of the gamma prime fraction on the gamma/gamma prime topological inversion during high temperature creep of single crystal super alloys, in: R.C. Reed, et al. (Eds.), *Superalloys 2008*, Proc. of the 11th International Symposium on Superalloys, TMS, Warrendale, 2008, pp. 159–167.
- [63] J.B. le Graverend, J. Adrien, J. Cormier, Ex-situ X-ray tomography characterization of porosity during high-temperature creep in Ni-based single-crystal superalloy: toward understanding what is damage, *Mater. Sci. Eng., A* 695 (2017) 367–378.
- [64] J. Cormier, P. Villechaise, X. Milhet,  $\gamma'$ -phase morphology of Ni-based single crystal superalloys as an indicator of the stress concentration in the vicinity of pores, *Mater. Sci. Eng., A* 501 (2009) 61–69.
- [65] F. Touratier, E. Andrieu, D. Poquillon, B. Viguier, Rafting microstructure during creep of the MC2 nickel-based superalloy at very high temperature, *Mater. Sci. Eng., A* 510–511 (2009) 244–249.
- [66] M. Gebura, J. Lapin, The effect of multiaxial stress state on formation of rafts in CMSX-4 superalloy during creep, *Adv. Mater. Res.* 278 (2011) 222–227.
- [67] D.A. Porter, K.E. Easterling, *Phase Transformations in Metals and Alloys*, 2th Edition, Reprinted by Nelson Thornes Ltd, Cheltenham, UK, 2001. Chapman & Hall, London, 1992.